Tumor Cell–Intrinsic USP22 Suppresses Antitumor Immunity in Pancreatic Cancer

Jinyang Li[1,2,3,4], Salina Yuan[1,2,3,4], Robert J. Norgard[1,2,3,4], Fangxue Yan[4,5], Taiji Yamazoe[1,2,3], Andrés Blanco[4,5], and Ben Z. Stanger[1,2,3,6]

ABSTRACT

Although immune checkpoint blockade (ICB) improves clinical outcome in several types of malignancies, pancreatic ductal adenocarcinoma (PDA) remains refractory to this therapy. Preclinical studies have demonstrated that the relative abundance of suppressive myeloid cells versus cytotoxic T cells determines the efficacy of combination immunotherapies, which include ICB. Here, we evaluated the role of the ubiquitin-specific protease 22 (USP22) as a regulator of the immune tumor microenvironment (TME) in PDA. We report that deletion of USP22 in pancreatic tumor cells reduced the infiltration of myeloid cells and promoted the infiltration of T cells and natural killer (NK) cells, leading to an improved response to combination immunotherapy. We also showed that ablation of tumor cell–intrinsic USP22 suppressed metastasis of pancreatic tumor cells in a T-cell–dependent manner. Finally, we provide evidence that USP22 exerted its effects on the immune TME by reshaping the cancer cell transcriptome through its association with the deubiquitylase module of the SAGA/STAGA transcriptional coactivator complex. These results indicated that USP22 regulates immune infiltration and immunotherapy sensitivity in preclinical models of pancreatic cancer.

Introduction

Immune checkpoint blockade (ICB) has led to improved clinical outcomes in several types of cancer (1, 2). However, the majority of patients treated with ICB fail to respond, leading to overall response rates of 20% to 40% (2). The abundance of tumor-infiltrating T cells is a major factor predicting response to immunotherapy, as T-cell–inflamed tumors are more sensitive to ICB than non-T-cell–inflamed tumors (3). Thus, there is an urgent need to understand the factors regulating intratumoral T-cell infiltration. Studies have shown that the tumor mutational burden does not fully explain the abundance of tumor-infiltrating T cells (4), and there is an increasing agreement that various tumor cell–intrinsic factors, including signaling molecules, secreted factors, and transcriptional regulators, influence the level of T-cell infiltration into tumors and the resulting response to immunotherapy (5).

Pancreatic ductal adenocarcinoma (PDA) is predicted to become the second leading cause of cancer-related death in the United States within the next five years (6). Pancreatic tumors are characterized by T-cell exclusion and an immunosuppressive tumor microenvironment (TME). As a result, PDA is largely resistant to immunotherapy (7). We and others have reported that tumor cell–intrinsic factors–secreted molecules, signaling pathways, and epigenetic status–play a central role in shaping the immune TME in PDA and other types of cancer (5, 8–10). Importantly, heterogeneous mechanisms may contribute to the suppression of antitumor immunity (9). Several studies have demonstrated that a drug combination including gemcitabine, nab-paclitaxel, CD40 agonistic antibody, PD-1 blocking antibody, and CTLA-4 blocking antibody promotes positive outcomes in preclinical mouse models of PDA (9, 11, 12). Importantly, preclinical studies indicate that the abundance of tumor-infiltrating activated $CD8^+$ T cells predicts sensitivity to this therapy (9). In this study, we evaluated the behavior of ubiquitin-specific protease 22 (USP22) as a tumor cell—intrinsic factor shaping the immune TME in PDA.

Materials and Methods

Animals

All animal procedures were conducted following NIH guidelines. All mouse protocols were in accordance with, and with the approval of the Institutional Animal Care and Use committee (IACUC) of the University of Pennsylvania (Philadelphia, PA). All wild-type (WT) C57BL/6 mice were purchased from The Jackson Laboratory and/or bred at the University of Pennsylvania (Philadelphia, PA). Kras-LSL-G12D/+;Trp53-LSL-R172H/+, Pdx1-Cre, and Rosa-LSL-YFP (KPCY) mice were bred in-house, backcrossed for over 10 generations with C57BL/6J mice (Jackson Laboratories), and assessed at the DartMouse Speed Congenic Core facility at the Geisel School of Medicine at Dartmouth College.

Tumor cells

All mouse pancreatic tumor cell clones were tested by the Research Animal Diagnostic Laboratory (RADIL) at the University of Missouri (Columbia, MO), using the Infectious Microbe PCR Amplification Test (IMPACT) II. Tumor cells were cultured in DMEM (high glucose without sodium pyruvate) with 10% FBS (Gibco) and glutamine (2 mmol/L). The clones were regularly tested using the MycoAlert Mycoplasma Detection Kit (Lonza). Mouse pancreatic tumor cell clones 6419c5, 6694c2, and 6422c1 were generated in our laboratory (9)

[1]Department of Medicine, University of Pennsylvania, Philadelphia, Pennsylvania. [2]Department of Cell and Developmental Biology, University of Pennsylvania, Philadelphia, Pennsylvania. [3]Abramson Family Cancer Research Institute, University of Pennsylvania, Philadelphia, Pennsylvania. [4]Cell and Molecular Biology Graduate Group, University of Pennsylvania, Philadelphia, Pennsylvania. [5]Department of Biomedical Sciences, School of Veterinary Medicine, University of Pennsylvania, Philadelphia, Pennsylvania. [6]Abramson Cancer Center, University of Pennsylvania, Philadelphia, Pennsylvania.

Note: Supplementary data for this article are available at Cancer Immunology Research Online (http://cancerimmunolres.aacrjournals.org/).

Corresponding Author: Ben Z. Stanger, University of Pennsylvania, Philadelphia, PA 19104. Phone: 215-746-5560; Fax: 215-573-2486; E-mail: bstanger@upenn.edu

Cancer Immunol Res 2020;8:282–91

doi: 10.1158/2326-6066.CIR-19-0661

and were used for less than 18 passages. These tumor cell clones were derived from the KPCY mice (as described above) and, thus, expressed YFP at the time of generation. We used 293T cells (ClonTech, 632180) for lentivirus packaging.

Implantation of tumor cells

Pancreatic tumor cells (as described above in the "Tumor cells" section) were dissociated into single cells with 0.25% trypsin (Gibco), washed with serum-free DMEM twice, and counted in preparation for subcutaneous or orthotopic implantations. A total of 2.0×10^5 tumor cells were implanted subcutaneously and 5.0×10^4 tumor cells were implanted orthotopically into the pancreas of 6- to 8-week-old female C57BL/6 mice via laparotomy as described previously (9). Tumors were harvested 18–24 days following implantation. Endpoint criteria included tumor volume exceeding 500 mm^3, severe cachexia, or weakness and inactivity.

Subcutaneous tumor growth and regression assessments

For tumor growth kinetics, tumors were measured every 3 days. Tumor length and width were measured with calipers, and tumor volumes were then calculated as length $\times$ $width^2/2$. Tumor volumes of 500 mm^3 were used as an endpoint for survival analysis. Tumor regressions and were calculated using the initial tumor size at the start of treatment to tumor size 15 days later.

Lung metastatic colonization assay

A total of 1.0×10^5 Usp22-WT and Usp22 knockout (Usp22-KO) tumor cells were injected via tail vein into C57BL/6 mice. After 14 days, lungs were harvested, weighed, and subjected to flow cytometry for immune profiling as described below in the flow analysis section. The tail vein injection experiment was performed in one experiment for each using two CRISPR KO clones, with 5 mice per group for analysis.

Treatments and T-cell depletions in C57BL/6J mice

Gemcitabine (Hospira) and nab-paclitaxel (Abraxane; Celgene) were purchased from the Hospital of the University of Pennsylvania Pharmacy. Gemcitabine (G) was procured as pharmaceutical grade suspension at 38 mg/mL, and further diluted to 12 mg/mL in PBS and administered at 120 mg/kg via intraperitoneal injection. Abraxane (A) was purchased as a pharmaceutical-grade powder resuspended at 12 mg/mL in PBS for intraperitoneal injection at dose of 120 mg/kg. Vehicle control mice received the equivalent to nab-paclitaxel dose of human albumin (huAlb; Sigma). Chemotherapy was injected when tumor was 3 to 5 mm. For anti-CD40 agonist treatment, mice were injected intraperitoneally with 100 μg of either agonistic CD40 rat anti-mouse IgG2a (clone FGK45, endotoxin free) or the isotype control IgG2a (clone 2A3, Bio X Cell) 48 hours after chemotherapy. For checkpoint blockade treatment, mice were injected intraperitoneally with 200 μg of anti–PD-1 (clone RMP 1-14, Bio X Cell) and 200 μg anti–CTLA-4 (clone 9H10, Bio X Cell), starting day 10 (therapy start timepoint), with six and three doses, respectively. Control mice received the isotype control IgG2a (clone 2A3, Bio X Cell) on treatment days. $CD4^+$ and $CD8^+$ T cells were depleted using intraperitoneal injections of 200 mg anti-CD4 (clone GK1.5, Bio X Cell) and anti-CD8 (clone 2.43, Bio X Cell), three days prior tumor implantation, and three times a week for the duration of the experiment. Control groups received IgG2b isotype control (Bio X Cell). The treatment experiment was performed in one experiment for each using two CRISPR KO clones, with 7 to 8 mice per group for analysis.

Analysis of RNA sequencing, differential gene expression, gene set enrichment analysis, and EnrichR analysis

RNA sequencing (RNA-seq) data is deposited at GEO (GSE140088). RNA samples were extracted from sorted YFP^+ tumor cells from subcutaneous tumors 21 days postimplantation using the Qiagen RNeasy Micro Kit following manufacturer's instructions. RNA was sent to Novogene, for library preparation and high-throughput sequencing using Illumina sequencers (Hiseq 2500) to generated paired-end 150 bp data. Fastq files were checked for quality using FastQC (Babraham). Raw counts of gene transcripts were obtained using alignment-independent tool, Salmon (https://combine-lab.github.io/salmon/), using standard settings. The raw count matrix was subsequently imported into R-studio (R version 3.3.3) and used as input for DESeq2 following the vignette of the package for normalization and differential gene expression analysis. Salmon was also used to normalize and quantitate gene expression in transcripts-per-million (tpm) through quasi-alignment. Differentially expressed genes from the DESeq2 analysis were used as input for MSigDB gene set enrichment analysis (GSEA). Differentially expressed genes ($P_{adj} < 0.01$ and absolute fold change > 2) were used as input for EnrichR analysis (ENCODE and ChEA Consensus TFs from ChIP-X and ChEA datasets).

Lentiviral transduction of tumor cells for short hairpin RNA–mediated knockdown and CRISPR-mediated ablation

The short hairpin RNA (shRNA) knockdown vector, pLKO.1.puro, was a gift from Robert Weinberg (Addgene plasmid #8453). The CRISPR vector, lentiCRISPR v2, was a gift from Feng Zhang (Addgene plasmid # 52961). The vector and pVSVg and psPAX2 lentiviral packaging plasmids (Addgene) were cotransfected into 293T cells (ClonTech, 632180) using PEI reagent (Polysciences, 23966-2). Lentiviral particles were collected 48 or 72 hours after transfection and filtered for usage. Tumor cells transduced either with Cas9-Puro (control) or Cas9-guide-Puro (KO; control is from Addgene, #52961, and KOs were cloned following the instruction from Addgene) were selected with 8 μg/mL puromycin (Invitrogen, A1113803). Single-cell clones were picked from bulk KO cell line using single-cell sorting using a BD Jazz FACS sorter into 96-well plates. KO efficiencies were assessed by gene-specific qPCR analysis and immunofluorescence to detect target proteins (staining methods described below). shRNA sequences used were:

Atxn7l3-sh1-F-
CCGG-AGGCGAACCGTACGGATTTAT-CTCGAG-
ATAAATCCGTACGGTTCGCCT-TTTTTG;
Atxn7l3-sh1-R-
AATT-CAAAAA-AGGCGAACCGTACGGATTTAT-
CTCGAG-ATAAATCCGTACGGTTCGCCT; Atxn7l3-sh2-F-
CCGG-TCGAAGATCCAAGTCTCTAAA-CTCGAG-TTTA-
GAGACTTGGATCTTCGATTTTTG; Atxn7l3-sh2-R-
AATT-CAAAAA-TCGAAGATCCAAGTCTCTAAA-
CTCGAGTTTAGAGACTTGGATCTTCGA.

CRISPR sgRNA sequences used were:

Usp22-A-TCT-GCG-TGG-ACT-GAT-CAA-CC;
Usp22-B-AGT-TCC-AGC-TCC-CGT-TTA-GT.

Quantitative PCR analysis for gene expression

RNA was prepared from cultured tumor cells using RNeasy Mini Kit or RNeasy Micro Kit (Qiagen). cDNA was generated using High-capacity cDNA Reverse Transcription Kit from 1 μg RNA in 20 μL

reaction volume and diluted 1:10 for qPCR analysis (Life Technologies). qPCR analysis was performed using 2 μL diluted cDNA with biological (2–3) and technical replicates (2–3) using SsoAdvanced SYBR reagent (Bio-Rad) and Bio-Rad qPCR platform, and results were normalized to the expression of *Tbp* using the Bio-Rad software. Primer sequences utilized for qPCR were: Usp22-F-CTC-CCC-ACA-CAT-TCC-ATA-CAA-G; Usp22-R-TGG-AGC-CCA-CCC-GTA-AAG-A; Atxn7l3-F-TTG-TCT-GGC-CTG-GAT-AAC-AGC; Atxn7l3-R-CCG-GTG-TAC-TTC-AAA-GCA-GAA-TC; Tbp-F-AGA-ACA-ATC-CAG-ACT-AGC-AGC-A; Tbp-R-GGG-AAC-TTC-ACA-TCA-CAG-CTC.

Flow cytometry of implanted tumors and lung

For the flow cytometric analyses, subcutaneous or orthotopic tumors following 18–24 days of implantation were chopped into small pieces and digested in collagenase (1 mg/mL in DMEM; Sigma-Aldrich) at 37°C for 45 minutes and filtered through a 70-μm cell strainer. Single-cell suspensions were stained with antibodies on ice for 30 minutes and washed twice with PBS with 5% FBS for flow cytometric analysis. No intracellular staining is needed for this analysis. Cells were then analyzed by flow cytometry using BD FACS (BD Biosciences) and FlowJo software (Treestar).

The following antibodies used were for the analysis: CD279 (PD-1) FITC (29F.1A12; BioLegend 135214), CD335 (NKp46) PE (29A1.4; BioLegend 137604), CD103 PE/Dazzle 594 (2E7; BioLegend 121430), CD3e PE/Cy5 (145-2C11; BioLegend 100310), CD45 AF700 (30-F11; BioLegend 103128), CD8a PE/Cy7 (53-6.7; BioLegend 100722), I-A/I-E (MHCII) PE/Cy7 (M5/114.15.2; BioLegend 107630), Ly-6G V450 (1A8; BD Biosciences 560603), H-2Kb/H-2Db (MHCI) AF647 (28-8-6; BioLegend 114612), F4/80 APC/Cy7 (BM8; BioLegend 123118), CD11b PerCP-Cy5.5 (M1/70; BD Biosciences 550993), CD11c BV605 (N418; BioLegend 117334), Ly-6C BV570 (HK1.4; BioLegend 128030), and CD4 BV650 (RM4-5; BioLegend 100546).

The following gating strategies were used for immune cells: myeloid cells—live $CD45^+CD11b^+$; granulocytic myeloid-derived suppressor cells (gMDSC)/neutrophils—live $CD45^+CD11b^+Gr1^+$; macrophages—live $CD45^+F4/80^+CD11b^+$; $CD11c^+$ dendritic cells (DC)—live $CD45^+F4/80^-$ $CD11c^+$; $CD103^+$ DCs—live $CD45^+CD11b^-F4/80^-CD11c^+$ $CD103^+$; T cells—live $CD45^+CD11b^-F4/80^-NKp46^-CD3^+$; $CD4^+$ T cells—live $CD45^+CD11b^-F4/80^-NKp46^-CD3^+CD4^+$; $CD8^+$ T cells—live $CD45^+CD11b^-F4/80^-NKp46^-CD3^+CD8^+$. The flow analysis of immune infiltration of USP22-WT versus KO tumors were performed in two experiments using six CRISPR KO clones, with 4 to 5 mice per tumor cell clone.

Flow cytometry of *in vitro* tumor cells for EdU

Tumor cells were incubated with EdU for 3 hours in DMEM with 10% FBS and Glutamax (Thermo Fisher Scientific 35050061) and then fixed with fixation buffer following the instruction of the reagent (eBioscience 00-5123-43 and 00-5223-56). Samples were further processed for EdU staining as per protocol (Thermo Fisher Scientific, C10086). Samples were stained for EdU and then analyzed by flow cytometry using BD FACS LSR machine (BD Biosciences) and FlowJo software (Treestar).

In vitro treatment with IFNγ for MHC I expression analysis

Usp22-WT and Usp22-KO tumor cells were treated with 100 ng/mL of IFNγ (PeproTech) in DMEM with 10% FBS and Glutamax (Thermo Fisher Scientific 35050061) for 24 hours. Tumor cells were trypsinized from culture plates and resuspended in PBS with 5% FBS for staining of antibodies. Single-cell suspensions were stained with antibodies on ice for 30 minutes and washed twice with PBS with 5% FBS for flow cytometric analysis. Samples were stained for MHCI (BioLegend 114612) and then analyzed by flow cytometry using BD FACS LSR machine (BD Biosciences) and FlowJo software (Treestar).

Immunofluorescent and IHC staining

For CD3, USP22, and Gr1 staining, collected implanted tumor tissues were fixed in Zn-formalin for 24 hours and embedded in paraffin. Sections were deparaffinized, rehydrated, and prepared by antigen retrieval for 6 minutes each, and then blocked in 5% donkey serum (Sigma, D9663) for 1 hour at room temperature, incubated with primary antibodies overnight at 4°C, washed with 0.1% PBST (PBS with Tween-20), incubated with secondary antibodies for 1 hour at room temperature, and then washed and mounted. Slides were visualized and imaged using an Olympus IX71 inverted multicolor fluorescent microscope and a DP71 camera. For CD3 and Gr1 staining quantification, stained cells were counted for $CD3^+$ T cells manually in 5–8 fields per sample.

The following primary antibodies: CD3 (Abcam ab5690, 1:100 dilution), USP22 (Abcam ab195289, 1:100 dilution), Gr-1 (eBioscience 1:50 ,85-5931-14 dilution), YFP (Abcam, ab6673). Secondary antibodies were purchased from Invitrogen (A-11055, A-21207, A-21209) and were used as 1:250 dilution for all staining.

Cancer Dependency Map portal (DepMap) data analysis

The DepMap portal (https://depmap.org/portal/) and the CRISPR (Avana) Public 19Q3 dataset were used for this analysis. No samples were excluded from the dataset, and 625 cell lines in total were included in this analysis. Following the DepMap instruction, the dependency scores of genes were downloaded and plotted as dot plots. Pearson correlation was calculated for all the plots using Prism.

Statistical analysis

Statistical comparisons between two groups were performed using Student unpaired *t* test. For comparisons between multiple groups, one-way ANOVA with Tukey's HSD post-test was used. For survival comparison between two groups, log-rank *P* values of Kaplan–Meier curves were determined in GraphPad Prism 8 (GraphPad). On graphs, error bars represent either range or SEM, as indicated in legends. For all figures, $P < 0.05$ was considered statistically significant; *, $P < 0.05$; **, $P < 0.01$; ***, $P < 0.001$.

Software

PRISM software and R were used for the data processing, statistical analysis, and result visualization (http://www.graphpad.com). The R language and environment for statistical computing and graphics (https://www.r-project.org) was utilized in this study for the statistical and bioinformatics analysis of RNA-seq data. The R packages used for all analysis described in this manuscript were obtained from the Bioconductor and CRAN.

Results

Tumor cell–intrinsic USP22 regulates immune cell infiltration in implanted PDA tumors

We previously established an experimental system that recapitulates the heterogeneity of immune cell infiltration in pancreatic cancer (9). This platform consists of a group of primary murine PDA tumors stratified into two main subsets: a T-cell–low group, enriched for myeloid-derived suppressor cells (MDSC), and a T-cell–high group, enriched for T cells and DCs, with reduced MDSCs. We and others

have previously demonstrated that several tumor cell–intrinsic factors, including CSF2, CXCL1, CSF3, EPHA2, and PTGS2, can control the abundance of tumor-infiltrating myeloid cells and T cells, which, in turn, affects the sensitivity of PDA tumors to combination immunotherapy (8). In these studies, we found that mechanisms underlying the establishment of the non-T-cell–inflamed TME varied from tumor to tumor. Here, we aimed to identify alternative tumor cell–intrinsic regulators of the immune TME that might lead to novel therapeutic targets for precision immunotherapy.

Ablation of USP22 in liver tumor cells has been shown to increase tumor immunogenicity and promote infiltration of T cells into the resulting liver tumors (13). An examination of our PDA clone library revealed that T-cell–low tumors expressed higher USP22 at the RNA and protein level compared with T-cell–high tumors (Supplementary Fig. S1A and S1B). These findings are consistent with the idea that USP22 promotes the non-T-cell–inflamed TME and suppresses antitumor immunity in PDA. To functionally examine the role of USP22 in regulating the immune TME, we utilized CRISPR/Cas9 strategy to generate six independent *Usp22*-KO cell clones (Supplementary Fig. S1C) from a well-established T-cell–low PDA tumor cell clone, 6419c5. We then performed flow cytometric analysis to assess the phenotype of immune cells that infiltrated into subcutaneously implanted *Usp22*-WT and *Usp22*-KO tumors. USP22 ablation resulted in decrease in total myeloid cells and gMDSCs and an increase in $CD3^+$, $CD4^+$, and $CD8^+$ T cells in the TME (**Fig. 1A** and **B**). $CD8^+$ T cells in *Usp22*-KO tumors were more frequently positive for CD44 and PD-1 (**Fig. 1C**). These changes in myeloid and T-cell populations within the TME were confirmed by immunofluorescence staining of CD3 and Gr1 (**Fig. 1D** and **E**). *Usp22*-KO tumors also exhibited increased natural killer (NK)–cell infiltration but no significant change in the number of macrophages or DCs (Supplementary Fig. S1D).We also observed a minor decrease of tumor growth *in vivo* and 10% decrease of EdU incorporation *in vitro* following ablation of USP22 (Supplementary Fig. S1E and S1F), consistent with previous reports

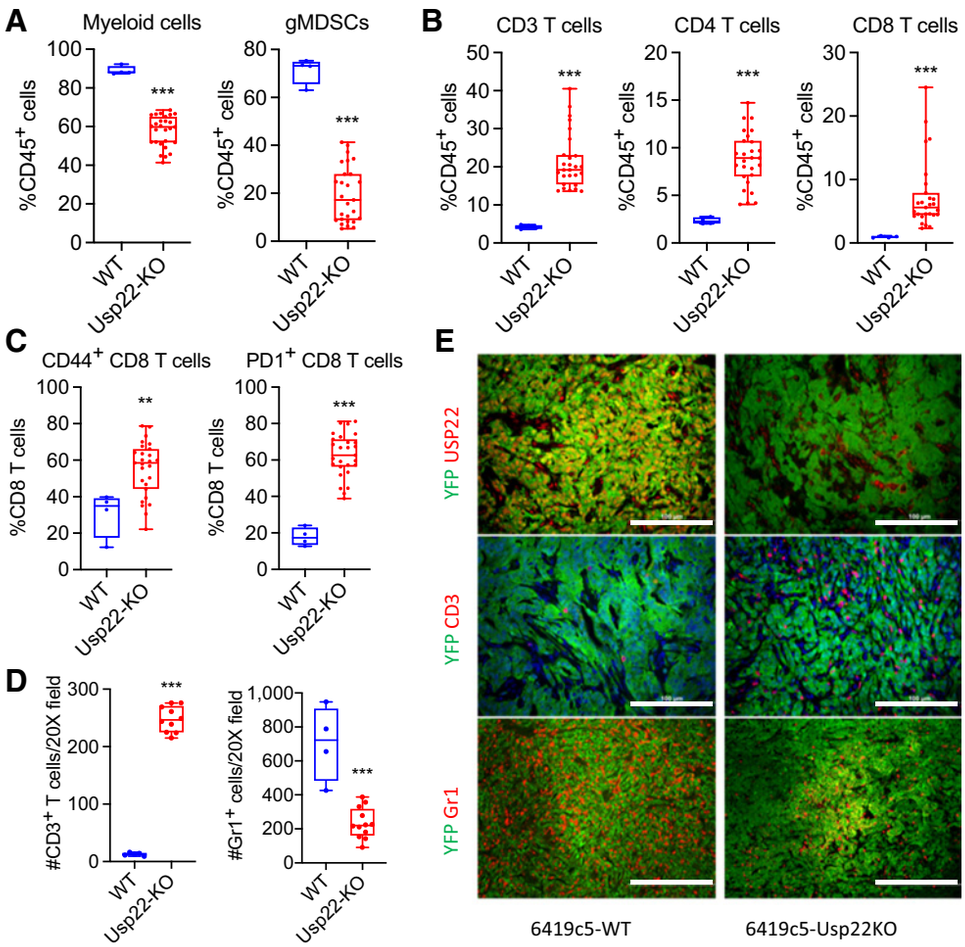

Figure 1.

Loss of tumor cell–intrinsic USP22 increases T-cell infiltration and decreases myeloid cell infiltration in subcutaneously implanted PDA tumors. **A–C,** Flow cytometric analysis of tumor-infiltrating immune cells in subcutaneously implanted *Usp22*-WT and *Usp22*-KO (six independent KO tumor cell clones, $n = 4$–27 tumors analyzed per group in three experiments). Quantification (**D**) and representative immunofluorescent staining images (**E**, middle and bottom) of $CD3^+$ T cells and $Gr1^+$ myeloid cells in *Usp22*-WT and *Usp22*-KO tumors (two independent KO clones, $n = 4$–12 tumors analyzed per group) stained for CD3 or Gr1 (red), YFP (green), and DAPI (blue). **E,** Top, representative image stained for USP22 (red) and YFP (green) in *Usp22*-WT or *Usp22*-KO tumors. In **A–D**, data are presented as boxplots with horizontal lines and error bars indicating mean and range, respectively. Statistical differences between groups were calculated using Student unpaired *t* test *, $P < 0.05$; **, $P < 0.01$; ***, $P < 0.001$. Scale bars, 100 μm for CD3 and USP22; 200 μm for Gr1.

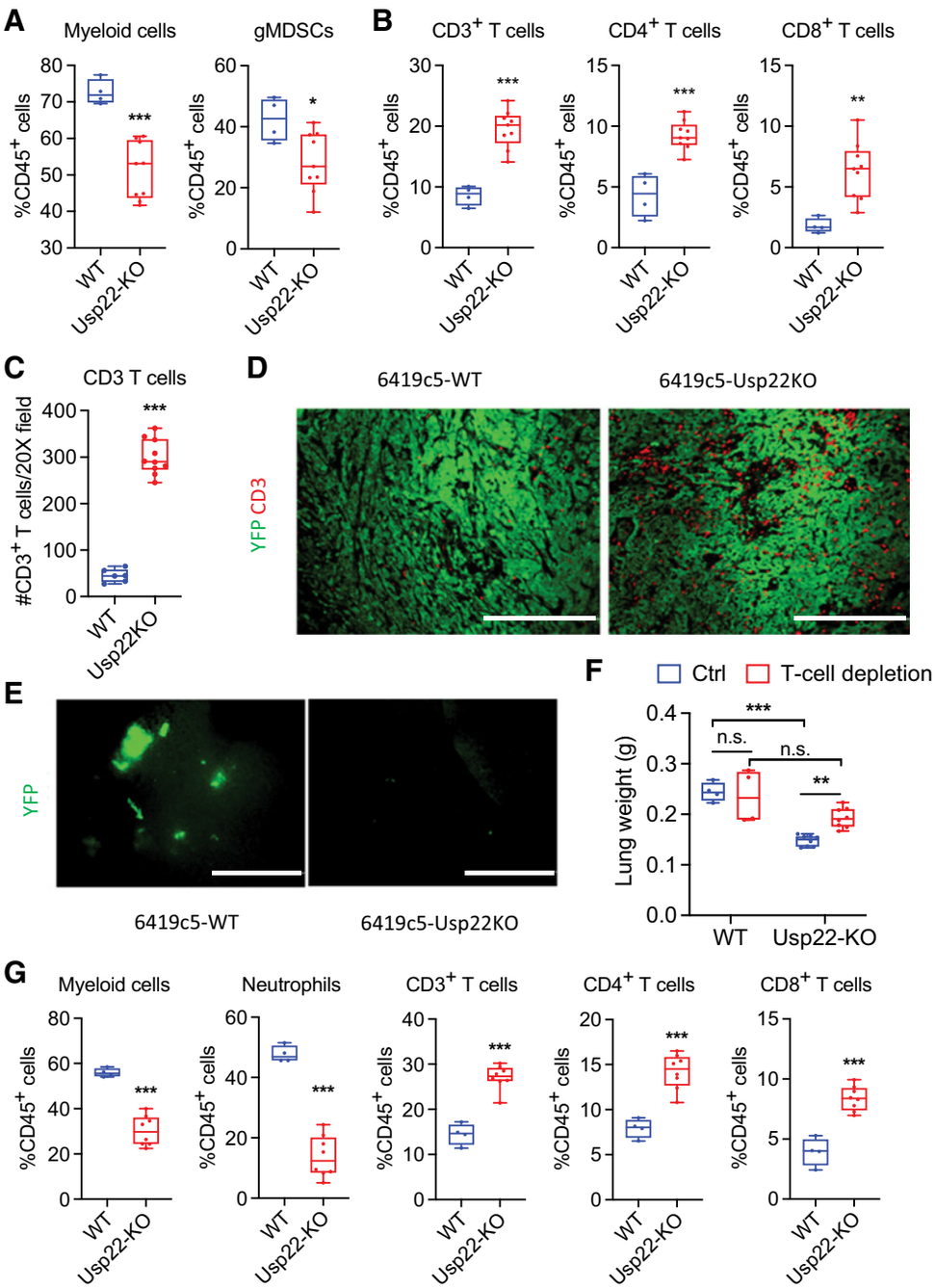

Figure 2.

Loss of tumor cell–intrinsic USP22 promotes antitumor immunity in orthotopic PDA tumors and suppresses lung metastasis. **A** and **B,** Flow cytometric analysis of tumor-infiltrating immune cells in orthotopically implanted *Usp22*-WT and *Usp22*-KO tumors (two independent KO clones, $n = 4$–9 tumors analyzed per group in two experiments). Quantification (**C**) and representative immunofluorescent staining (**D**) of $CD3^+$ T cells in *Usp22*-WT and *Usp22*-KO orthotopic tumors (two independent KO clones, $n = 6$–10 tumors analyzed per group) stained for CD3 (red) and YFP (green). **E,** Representative images of lungs from animals in **D**, with YFP^+ tumor cells shown in green. **F,** Quantification of lung weight 14 days after tail vein injection of *Usp22*-WT or *Usp22*-KO tumor cells (two independent KO clones) with or without T-cell depletion ($n = 5$ mice/group). **G,** Flow cytometric analysis of lungs following tail veil injection of *Usp22*-WT or *Usp22*-KO tumor cells (two independent KO clones, $n = 5$–10 mice/group in one experiment). In **A–C** and **F** and **G**, data are presented as boxplots with horizontal lines and error bars indicating mean and range, respectively. In **A–C** and **G**, statistical differences between groups were calculated using Student unpaired *t* test. In **F**, statistical differences between groups were calculated using two-way ANOVA analysis with multiple comparison (*, $P < 0.05$; **, $P < 0.01$; ***, $P < 0.001$). Scale bars, 200 μm in **D** and 1 mm in **E**. Ctrl, control; n.s., not significant.

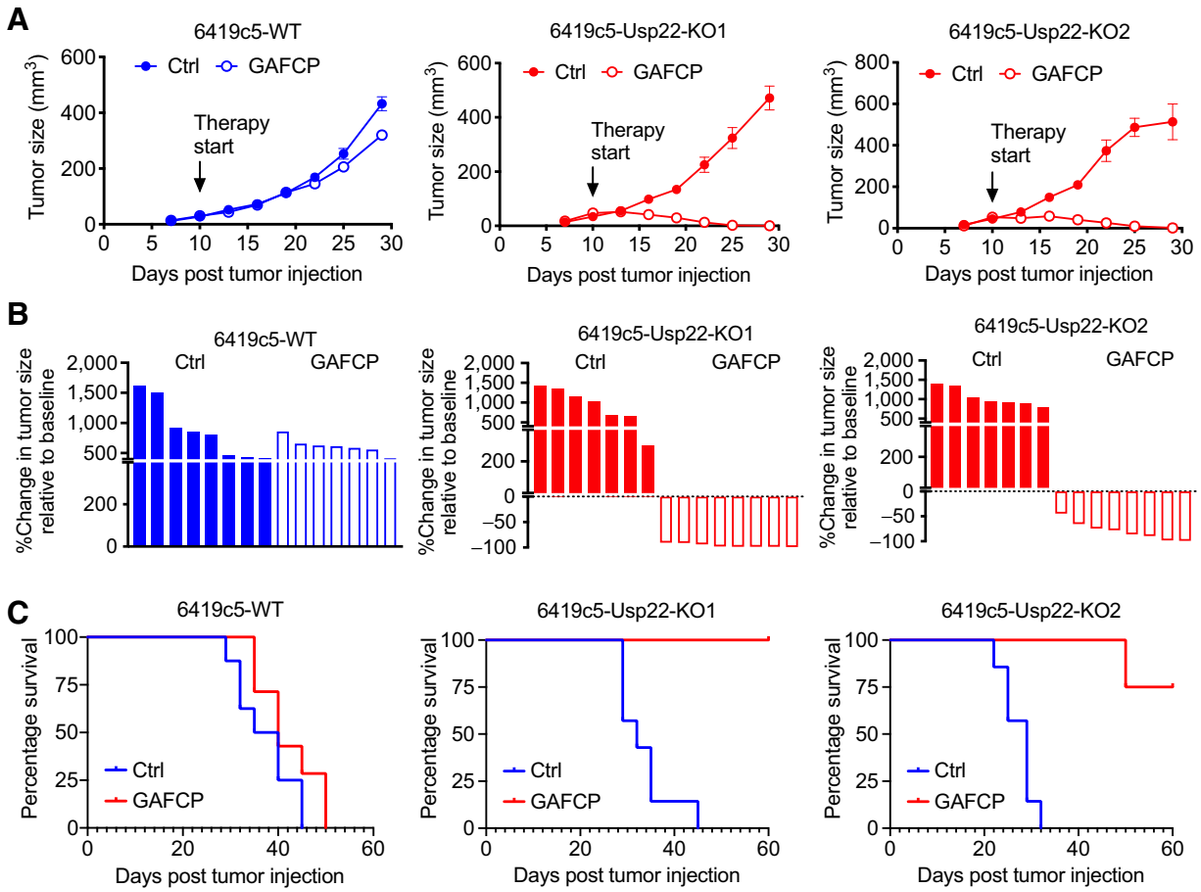

Figure 3.

USP22 loss increases the sensitivity of implanted PDA tumors to a combined immunotherapy. **A,** Growth curves (error bars, SEM) of *Usp22*-WT or *Usp22*-KO tumors with or without GAFCP treatment. Therapy was started on day 10 after implantation, when tumors were 3 to 5 mm in diameter. **B,** Waterfall plots from the cohort in **A** showing change in size of *Usp22*-WT and *Usp22*-KO tumors relative to the baseline (day 10) measured 15 days after treatment with or without GAFCP. **C,** Survival of animals from the cohort with *Usp22*-WT or *Usp22*-KO tumors with or without GAFCP treatment. Tumor cells implanted subcutaneously into C57BL/6 mice (n = 7–8/group; *, $P < 0.05$; **, $P < 0.01$; ***, $P < 0.001$). Ctrl, control.

suggesting that USP22 regulates cell-cycle progression and tumor growth (14–16). Likewise, T-cell depletion had no effect on the growth of either *Usp22*-WT or *Usp22*-KO tumors (Supplementary Fig. S1G and S1H), suggesting that the growth effects of *Usp22* ablation are not T-cell–dependent.

To expand these observations to other tumors, we generated *Usp22* KOs from two other T-cell–low tumor cell clones, 6422c1 and 6694c2. Flow analysis of the implanted tumors showed that loss of tumor cell–intrinsic USP22 decreased the abundance of gMDSCs and increased the number of $CD3^+$ and $CD4^+$ T cells in the TME of both 6422c1 and 6694c2 tumors (Supplementary Fig. S1I–S1L). A nonsignificant trend toward increased $CD8^+$ T cells was seen in *Usp22*-KO 6422c1 tumors (Supplementary Fig. S1H, right) and no difference seen in *Usp22*-KO 6694c2 tumors (Supplementary Fig. 1J, right). These results suggested that different T-cell–low tumors depended on USP22 to regulate $CD8^+$ T-cell infiltration to different degrees, further highlighting the importance of identifying patient-specific regulators of the immune TME.

Next, we assessed the infiltration of immune cells in tumors arising from 6419c5 *Usp22*-WT and *Usp22*-KO tumors that were orthotopically injected into the pancreas. Flow cytometry and immunofluorescence staining revealed that *Usp22* deletion resulted in a significant decrease of total myeloid cells and gMDSCs and an increase of $CD3^+$, $CD4^+$, and $CD8^+$ T cells in the TME, reproducing the findings from subcutaneous tumors (**Fig. 2A–D**; Supplementary Fig. S2A). Collectively, these results indicated that tumor cell–intrinsic USP22 establishes a non-T-cell–inflamed immune TME dominated by myeloid cells and a paucity of tumor-infiltrating T cells.

USP22 regulates T-cell–dependent lung metastasis

Studies have demonstrated the significant role of both adaptive and innate immune cells in regulating the metastasis of tumor cells, including pancreatic tumor cells (9, 17). Using the orthotopic model, we observed that mice injected with 6419c5 *Usp22*-KO tumors harbored fewer lung metastases compared with mice injected with 6419c5 *Usp22*-WT tumors (**Fig. 2E**). To functionally examine the effect of tumor cell–intrinsic USP22 on lung metastatic colonization, we performed tail vein injection of *Usp22*-WT and *Usp22*-KO tumor cells into immunocompetent mice and observed that *Usp22*-KO tumor cells resulted in decreased metastatic burden compared with the *Usp22*-WT tumor cells (**Fig. 2F**). T-cell depletion had no effect on metastatic burden in mice bearing *Usp22*-WT tumors but led to an increased

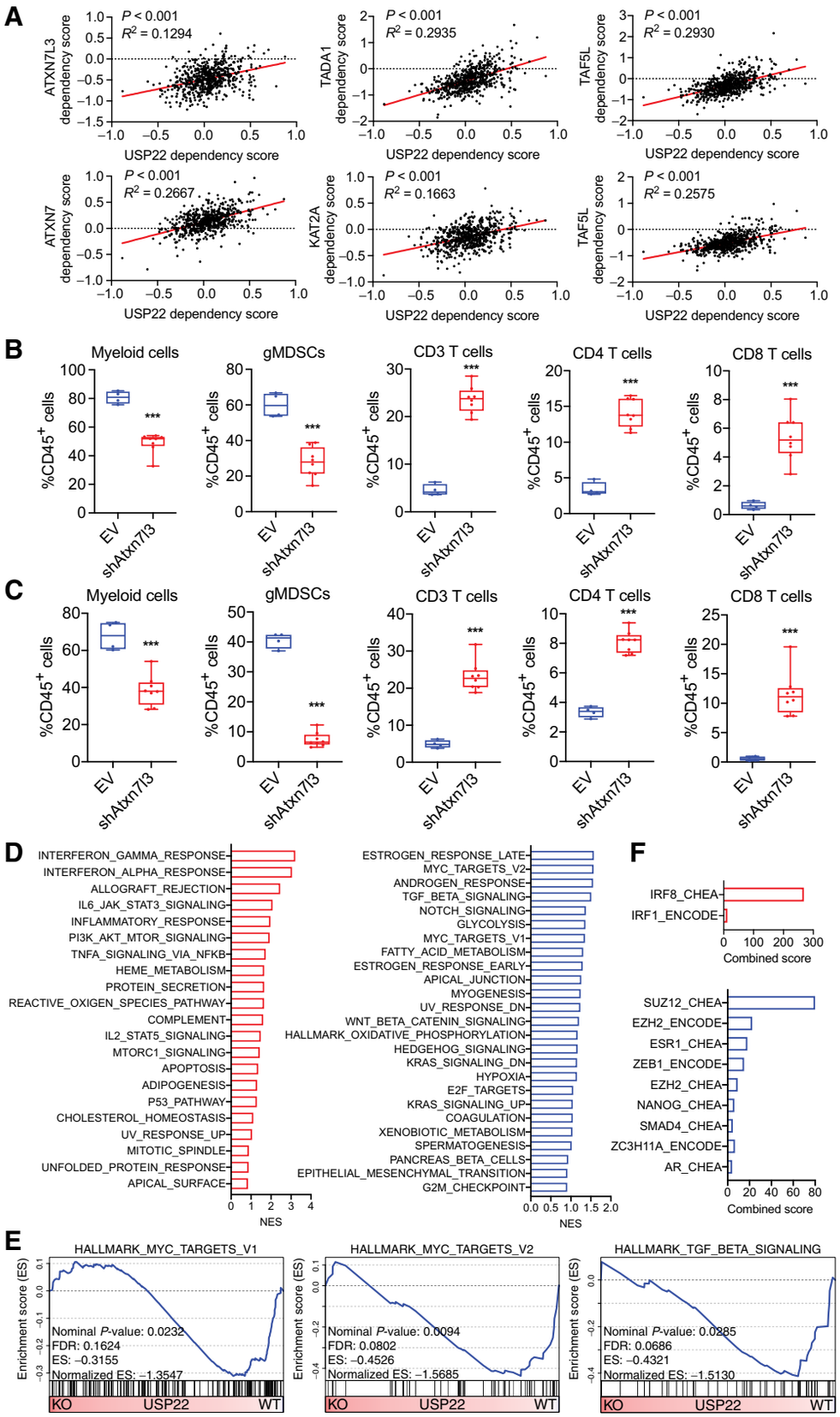

metastatic burden in mice bearing *Usp22*-KO tumor cells (**Fig. 2F**; Supplementary Fig. S2B). Metastatic lung lesions from *Usp22*-KO tumors exhibited fewer infiltrating myeloid cells and more T cells (**Fig. 2G**; Supplementary Fig. S2C). Similar results on metastatic burden and immune infiltration were seen when another T-cell–low tumor cell clone, 6694c2, was introduced by tail vein injection (Supplementary Fig. S2D and S2E). These results suggest that *Usp22*-KO tumor cells have a reduced ability to form metastases secondary to T-cell surveillance.

Tumor cell–intrinsic USP22 affects the sensitivity of PDA tumors to immunotherapy

We previously reported that relative to T-cell–high tumors, T-cell–low tumors have decreased sensitivity to combination immunotherapy with GAFCP (gemcitabine, G; nab-paclitaxel, A; anti-CD40 agonist, F; anti–CTLA-4, C; and anti–PD-1, P). A similar combination therapy, including chemotherapy, checkpoint blockade, and CD40 agonist is currently tested in two clinical trials for patients with PDA (NCT02588443, NCT03214250). Given that loss of tumor cell–intrinsic USP22 resulted in increased T-cell infiltration, we assessed the sensitivity of 6419c5 *Usp22*-WT and *Usp22*-KO tumors to this combination. *USP22*-deficient PDA tumor cells exhibited a significantly better response to GAFCP therapy, resulting in tumor regressions and prolonged survival (**Fig. 3A–C**). Collectively, these experiments suggest that USP22 expression in PDA tumors cells suppresses antitumor immunity and confers resistance to immunotherapy.

Ablation of USP22 leads to transcriptional reprogramming of tumor cells

USP22 has been reported to regulate the immune TME by controlling the protein stability of PD-L1 in liver tumor cells (13). Immunofluorescent staining revealed that USP22 protein is principally located in the nucleus of PDA tumor cells (**Fig. 1E**; Supplementary Fig. S1B; Supplementary Fig. S3A), consistent with data from the human protein atlas (18, 19). We, therefore, hypothesized that USP22 might influence tumor immunity through nuclear functions independent of its effects on PD-L1 protein stability.

USP22 is a major component of the SAGA/STAGA complex, a multiprotein complex involved in transcriptional regulation (14). As the major deubiquitylase in the deubiquitylation module of this complex, USP22 is thought to regulate transcription by controlling ubiquitin levels of two histones—H2A and H2B—as well as other transcription factors including c-MYC, thereby regulating their stabilization and/or activity (14, 20–25). Analyzing the data from the Cancer Dependency Map portal (DepMap), we found USP22 shared dependencies with other factors in the deubiquitylation module of the SAGA/STAGA complex, including ATXN7, ATXN7L3, KAT2A, TADA1, TAF5L, and TAF6L (**Fig. 4A**). To further explore whether these other components of the SAGA/STAGA complex regulated the immune TME, we used shRNA to generate 6419c5 *Atxn7l3*-knockdown cell lines and performed flow analysis on the resulting tumors. Knockdown of *Atxn7l3* resulted in a decrease in total myeloid cells and gMDSCs as well as an increase in $CD3^+$, $CD4^+$, $CD8^+$ T cells, NK cells, and DCs (**Fig. 4B**; Supplementary Fig. S3B and S3C). Likewise, *Atxn7l3*-knockdown tumors had a higher frequency of PD-1^+ $CD8^+$ T cells (Supplementary Fig. S3C). These results were confirmed by knocking down *Atxn7l3* in a second T-cell–low clone, 6694c2 (**Fig. 4C**; Supplementary Fig. S3D and S3E). These data suggested that at least one other component of the deubiquitylation module of the nuclear SAGA/STAGA complex, ATXN7L3, may regulate the immune TME of PDA tumors.

On the basis of these findings, we hypothesized that ablation of tumor cell–intrinsic USP22 would result in significant transcriptional changes in tumor cells, thereby contributing to USP22's regulation of the immune TME. We used a YFP-lineage marker to sort the cancer cells from implanted tumors and then performed RNA-seq. *Usp22*-WT and *Usp22*-KO tumor cells exhibited global differences in transcription (Supplementary Fig. S4A). GSEA of genes whose expression changed with *Usp22* loss revealed an enrichment of hallmark gene sets associated with naturally arising T-cell–low and T-cell–high tumor cells (9). Specifically, *Usp22*-KO tumor cells were enriched for IFN response signatures, whereas *Usp22*-WT tumor cells were enriched for MYC, TGFβ, and cell-cycle signatures (**Fig. 4D** and **E**; Supplementary Fig. S4B–S4D). We checked the expression of a group of factors regulating function and trafficking of myeloid cells and regulatory T cells and found that most of them were not significantly differentially expressed between *Usp22*-WT and *Usp22*-KO tumor cells. We found *Csf3* was significantly decreased in *Usp22*-KO tumor cells. In our previous publication (9), we identified CSF3 as one tumor cell–intrinsic regulator promoting the establishment of a non-T-cell–inflamed TME. One article (13) has demonstrated that USP22 can regulate PD-L1 at the posttranslational level to control tumor immunity in liver cancer. Here, we assessed the expression of both PD-L1 and MHCI on tumor cell surface with or without treatment of IFNγ and found that PD-L1 was not differentially expressed between *Usp22*-WT and *Usp22*-KO tumor cells (Supplementary Fig. S4E). However, consistent with our RNA-seq result, *Usp22*-KO tumor cells had increased expression of MHCI on cell surface compared with *Usp22*-WT tumor cells (Supplementary Fig. S4E). We then used the list of genes that were differentially expressed between *Usp22*-WT and *Usp22*-KO tumor cells as input for EnrichR (26, 27). EnrichR is an analytic tool that uses information from the Encyclopedia of DNA Elements (ENCODE) and ChIP-X Enrichment Analysis (ChEA) datasets to identify potential transcriptional regulators. This analysis revealed an enrichment of an IRF8 signature in *Usp22*-KO tumor cells (**Fig. 4F**; Supplementary Fig. S4F). This analysis nominated SUZ12 and EZH2, two key

Figure 4.

USP22 loss reprograms tumor cells toward a T-cell–high transcriptional program. **A,** Dot plots showing the dependency scores for the indicated members of the SAGA/STAGA complex relative to USP22 across all tumor cell line samples in the Cancer Dependency Map. **B,** Flow cytometric analysis of tumor-infiltrating immune cells in subcutaneously implanted 6419c5-EV- and 6419c5-Atxn7l3-knockdown tumors (two independent knockdown cell lines, $n = 4$–8 tumors analyzed per group in one experiment). **C,** Flow cytometric analysis of tumor-infiltrating immune cells in subcutaneously implanted 6694c2-EV- and 6694c2-Atxn7l3-knockdown tumors (two independent knockdown cell lines, $n = 4$–8 tumors analyzed per group in one experiment). **D,** Hallmark GSEA comparing differentially expressed genes in sorted *Usp22*-WT or *Usp22*-KO tumor cells ($n = 3$–6 tumors analyzed per group). Gene sets enriched in *Usp22*-KO tumor cells are labeled in red (left); gene sets enriched in *Usp22*-WT tumor cells are labeled in blue (right). NES, normalized enrichment score. **E,** Leading-edge plots from the GSEA highlighting three Usp22-WT tumor cell–enriched gene sets: Hallmark_MYC_targets_V1, Hallmark_MYC_targets_V2, and Hallmark_TGF_beta_signaling. **F,** Bar graphs showing predicted transcriptional regulators. Differentially expressed genes ($P_{adjusted} < 0.01$ and absolute fold change > 2) were used as input for EnrichR analysis (ENCODE and ChEA Consensus TFs from ChIP-X dataset). In **A**, data are presented as dot plots with the red line showing the linear regression result. Correlation metrics are shown. In **B** and **C**, data are presented as boxplots with horizontal lines and error bars indicating mean and range, respectively. Statistical differences between groups were calculated using Student unpaired *t* test (*, $P < 0.05$; **, $P < 0.01$; ***, $P < 0.001$).

components of the polycomb repressive complex 2 (PRC2 complex), as transcriptional regulators active in *Usp22*-WT tumor cells whose activity is lost following *Usp22* deletion (Supplementary Fig. S4F). Together, these evidences suggest potential mechanisms underlying USP22-mediated regulation of the immune TME of pancreatic cancer. Collectively, these data demonstrated that loss of tumor cell–intrinsic USP22 reprogramed the tumor cell transcriptome, resulting in a T-cell–high phenotype at molecular and cellular levels.

Discussion

Understanding the determinants of T-cell infiltration into tumors has important therapeutic implications. We and others have shown that regulatory factors operating in tumor cells play a central role in determining the makeup of their surrounding microenvironments (5, 8, 28). Here, we reported that USP22, a highly conserved component of the nuclear multiprotein SAGA/STAGA complex, is one such factor. These findings expand our understanding of tumor-intrinsic epigenetic factors that shape the TME (29, 30) and are in line with a report describing a role for USP22 in regulating the immune microenvironment in liver cancer (13).

The SAGA/STAGA complex promotes transcription, an activity mediated in part through a deubiquitylation module that contains USP22 and its binding partners ATXN7L3, ATXN7, and ENY2 (24, 31–34). We found that *Atxn7l3* knockdown phenocopied *Usp22* loss, supporting the notion that USP22-dependent effects on the immune microenvironment are mediated at least, in part, by the SAGA/STAGA complex. Deletion of *Usp22* associated with the decreased expression of genes enriched for consensus target gene signatures of SUZ12 and EZH2, two components of the repressive PRC2 complex. These findings raise the possibility that the SAGA/STAGA and PRC2 complexes act coordinately to regulate the activation and repression of genes that control the immune makeup of PDA tumors.

Usp22 is overexpressed in multiple tumor types, has been shown to regulate cell-cycle activity in association with cancer progression (14, 15, 35–38), and has been reported to play a role in antitumor immunity through the stabilization of PD-L1 in tumor cells (13). This study suggests that transcriptional regulation may be another mechanism by which *Usp22* controls the immune TME, thereby converting cells that are fully resistant to immunotherapy to a sensitive state. To date, no small-molecule inhibitors of USP22 have been reported, but given mounting evidence in multiple contexts that USP22 promotes tumor progression, the development of such inhibitors would be desirable. Such compounds may be useful in the context of novel immunotherapy combinations, such as those described in this study and currently under clinical investigation for PDA (NCT03214250).

Disclosure of Potential Conflicts of Interest

No potential conflicts of interest were disclosed.

Authors' Contributions

Conception and design: J. Li, R.J. Norgard, B.Z. Stanger
Development of methodology: J. Li, R.J. Norgard, B.Z. Stanger
Acquisition of data (provided animals, acquired and managed patients, provided facilities, etc.): J. Li, S. Yuan, F. Yan, T. Yamazoe, B.Z. Stanger
Analysis and interpretation of data (e.g., statistical analysis, biostatistics, computational analysis): J. Li, S. Yuan, R.J. Norgard, F. Yan, A. Blanco, B.Z. Stanger
Writing, review, and/or revision of the manuscript: J. Li, F. Yan, B.Z. Stanger
Administrative, technical, or material support (i.e., reporting or organizing data, constructing databases): J. Li, R.J. Norgard, F. Yan
Study supervision: B.Z. Stanger

Acknowledgments

This work was supported by grants from the NIH (R01-CA229803, to B.Z. Stanger) and the Blavatnik Family Foundation Fellowship (to J. Li). We thank members of the Stanger laboratories for technical help and scientific discussions.

The costs of publication of this article were defrayed in part by the payment of page charges. This article must therefore be hereby marked *advertisement* in accordance with 18 U.S.C. Section 1734 solely to indicate this fact.

Received August 28, 2019; revised November 6, 2019; accepted December 19, 2019; published first December 23, 2019.

References

1. Ribas A, Wolchok JD. Cancer immunotherapy using checkpoint blockade. Science 2018;359:1350–5.
2. Sanmamed MF, Chen L. A paradigm shift in cancer immunotherapy: from enhancement to normalization. Cell 2018;175:313–26.
3. Tumeh PC, Harview CL, Yearley JH, Shintaku IP, Taylor EJ, Robert L, et al. PD-1 blockade induces responses by inhibiting adaptive immune resistance. Nature 2014;515:568–71.
4. Spranger S, Luke JJ, Bao R, Zha Y, Hernandez KM, Li Y, et al. Density of immunogenic antigens does not explain the presence or absence of the T-cell-inflamed tumor microenvironment in melanoma. Proc Natl Acad Sci U S A 2016; 113:E7759–68.
5. Spranger S, Gajewski TF. Impact of oncogenic pathways on evasion of anti-tumour immune responses. Nat Rev Cancer 2018;18:139–47.
6. Rahib L, Smith BD, Aizenberg R, Rosenzweig AB, Fleshman JM, Matrisian LM. Projecting cancer incidence and deaths to 2030: the unexpected burden of thyroid, liver, and pancreas cancers in the United States. Cancer Res 2014;74: 2913–21.
7. Morrison AH, Byrne KT, Vonderheide RH. Immunotherapy and prevention of pancreatic cancer. Trends Cancer 2018;4:418–28.
8. Markosyan N, Li J, Sun YH, Richman LP, Lin JH, Yan F, et al. Tumor cell-intrinsic EPHA2 suppresses anti-tumor immunity by regulating PTGS2 (COX-2). J Clin Invest 2019;130:3594–609.
9. Li J, Byrne KT, Yan F, Yamazoe T, Chen Z, Baslan T, et al. Tumor cell-intrinsic factors underlie heterogeneity of immune cell infiltration and response to immunotherapy. Immunity 2018;49:178–93.
10. Bayne LJ, Beatty GL, Jhala N, Clark CE, Rhim AD, Stanger BZ, et al. Tumor-derived granulocyte-macrophage colony-stimulating factor regulates myeloid inflammation and T cell immunity in pancreatic cancer. Cancer Cell 2012;21: 822–35.
11. Byrne KT, Vonderheide RH. CD40 stimulation obviates innate sensors and drives T cell immunity in cancer. Cell Rep 2016;15:2719–32.
12. Winograd R, Byrne KT, Evans RA, Odorizzi PM, Meyer AR, Bajor DL, et al. Induction of T-cell immunity overcomes complete resistance to PD-1 and CTLA-4 blockade and improves survival in pancreatic carcinoma. Cancer Immunol Res 2015;3:399–411.
13. Huang X, Zhang Q, Lou Y, Wang J, Zhao X, Wang L, et al. USP22 deubiquitinates CD274 to suppress anti-cancer immunity. Cancer Immunol Res 2019;7:1580–90.
14. Melo-Cardenas J, Zhang Y, Zhang DD, Fang D. Ubiquitin-specific peptidase 22 functions and its involvement in disease. Oncotarget 2016;7:44848–56.
15. Zhang XY, Varthi M, Sykes SM, Phillips C, Warzecha C, Zhu W, et al. The putative cancer stem cell marker USP22 is a subunit of the human SAGA complex required for activated transcription and cell-cycle progression. Mol Cell 2008;29:102–11.
16. Lv L, Xiao XY, Gu ZH, Zeng FQ, Huang LQ, Jiang GS. Silencing USP22 by asymmetric structure of interfering RNA inhibits proliferation and induces cell cycle arrest in bladder cancer cells. Mol Cell Biochem 2011; 346:11–21.
17. Wculek SK, Malanchi I. Neutrophils support lung colonization of metastasis-initiating breast cancer cells. Nature 2015;528:413–7.

18. Uhlen M, Fagerberg L, Hallstrom BM, Lindskog C, Oksvold P, Mardinoglu A, et al. Proteomics. Tissue-based map of the human proteome. Science 2015;347:1260419.
19. Uhlen M, Zhang C, Lee S, Sjostedt E, Fagerberg L, Bidkhori G, et al. A pathology atlas of the human cancer transcriptome. Science 2017;357. pii: eaan2507.
20. Henry KW, Wyce A, Lo WS, Duggan LJ, Emre NC, Kao CF, et al. Transcriptional activation via sequential histone H2B ubiquitylation and deubiquitylation, mediated by SAGA-associated Ubp8. Genes Dev 2003;17:2648–63.
21. Kim D, Hong A, Park HI, Shin WH, Yoo L, Jeon SJ, et al. Deubiquitinating enzyme USP22 positively regulates c-Myc stability and tumorigenic activity in mammalian and breast cancer cells. J Cell Physiol 2017;232:3664–76.
22. Li L, Osdal T, Ho Y, Chun S, McDonald T, Agarwal P, et al. SIRT1 activation by a c-MYC oncogenic network promotes the maintenance and drug resistance of human FLT3-ITD acute myeloid leukemia stem cells. Cell Stem Cell 2014;15:431–46.
23. Bonnet J, Wang CY, Baptista T, Vincent SD, Hsiao WC, Stierle M, et al. The SAGA coactivator complex acts on the whole transcribed genome and is required for RNA polymerase II transcription. Genes Dev 2014;28:1999–2012.
24. Lang G, Bonnet J, Umlauf D, Karmodiya K, Koffler J, Stierle M, et al. The tightly controlled deubiquitination activity of the human SAGA complex differentially modifies distinct gene regulatory elements. Mol Cell Biol 2011;31:3734–44.
25. Zhang XY, Pfeiffer HK, Thorne AW, McMahon SB. USP22, an hSAGA subunit and potential cancer stem cell marker, reverses the polycomb-catalyzed ubiquitylation of histone H2A. Cell Cycle 2008;7:1522–4.
26. Kuleshov MV, Jones MR, Rouillard AD, Fernandez NF, Duan Q, Wang Z, et al. Enrichr: a comprehensive gene set enrichment analysis web server 2016 update. Nucleic Acids Res 2016;44:W90–7.
27. Chen EY, Tan CM, Kou Y, Duan Q, Wang Z, Meirelles GV, et al. Enrichr: interactive and collaborative HTML5 gene list enrichment analysis tool. BMC Bioinformatics 2013;14:128.
28. Li J, Stanger BZ. The tumor as organizer model. Science 2019;363:1038–9.
29. Sheng W, LaFleur MW, Nguyen TH, Chen S, Chakravarthy A, Conway JR, et al. LSD1 ablation stimulates anti-tumor immunity and enables checkpoint blockade. Cell 2018;174:549–63.
30. Peng D, Kryczek I, Nagarsheth N, Zhao L, Wei S, Wang W, et al. Epigenetic silencing of TH1-type chemokines shapes tumour immunity and immunotherapy. Nature 2015;527:249–53.
31. Sowa ME, Bennett EJ, Gygi SP, Harper JW. Defining the human deubiquitinating enzyme interaction landscape. Cell 2009;138:389–403.
32. Kohler A, Zimmerman E, Schneider M, Hurt E, Zheng N. Structural basis for assembly and activation of the heterotetrameric SAGA histone H2B deubiquitinase module. Cell 2010;141:606–17.
33. Samara NL, Datta AB, Berndsen CE, Zhang X, Yao T, Cohen RE, et al. Structural insights into the assembly and function of the SAGA deubiquitinating module. Science 2010;328:1025–9.
34. Zhao Y, Lang G, Ito S, Bonnet J, Metzger E, Sawatsubashi S, et al. A TFTC/STAGA module mediates histone H2A and H2B deubiquitination, coactivates nuclear receptors, and counteracts heterochromatin silencing. Mol Cell 2008;29:92–101.
35. Liang JX, Ning Z, Gao W, Ling J, Wang AM, Luo HF, et al. Ubiquitinspecific protease 22 induced autophagy is correlated with poor prognosis of pancreatic cancer. Oncol Rep 2014;32:2726–34.
36. Ning Z, Wang A, Liang J, Xie Y, Liu J, Feng L, et al. USP22 promotes the G1/S phase transition by upregulating FoxM1 expression via beta-catenin nuclear localization and is associated with poor prognosis in stage II pancreatic ductal adenocarcinoma. Int J Oncol 2014;45:1594–608.
37. Schrecengost RS, Dean JL, Goodwin JF, Schiewer MJ, Urban MW, Stanek TJ, et al. USP22 regulates oncogenic signaling pathways to drive lethal cancer progression. Cancer Res 2014;74:272–86.
38. Liu YL, Yang YM, Xu H, Dong XS. Increased expression of ubiquitin-specific protease 22 can promote cancer progression and predict therapy failure in human colorectal cancer. J Gastroenterol Hepatol 2010;25:1800–5.